



## A Replica Exchange Molecular Dynamics Simulation of a Single Polyethylene Chain: Temperature Dependence of Structural Properties and Chain Conformational Study at the Equilibrium Melting Temperature

Ting Li,<sup>†</sup> Xiaozhen Yang,<sup>‡</sup> and Erik Nies<sup>\*,†,§</sup>

*Polymer Research Division, Department of Chemistry, The Leuven Mathematical Modeling and Computational Science Centre (LMCC) and the Leuven Materials Research Centre (LMRC), Katholieke Universiteit Leuven, Celestijnenlaan 200F, B-3001 Heverlee, Belgium, State Key Laboratory of Polymer Physics & Chemistry, Center for Molecular Science, Institute of Chemistry, Chinese Academy of Sciences, Zhongguancun, Beijing 100080, Peoples' Republic of China, Laboratory of Polymer Technology, Eindhoven University of Technology, P.O. Box 513, 5600MB Eindhoven, The Netherlands*

Received September 10, 2010

**Abstract:** The conformational properties of a finite length polyethylene chain were explored over a wide range of temperatures using a replica exchange molecular dynamics simulation providing high quality simulation data representative for the equilibrium behavior of the chain molecule. The radial distribution function (RDF) and the structure factor  $S(q)$  of the chain as a function of temperature are analyzed in detail. The different characteristic peaks in the RDF and  $S(q)$  were assigned to specific distances in the chain and structural changes occurring with the temperature. In  $S(q)$ , a peak characteristic for the order in the solid state was found and used to determine the *equilibrium melting temperature*. A detailed scaling analysis of the structure factor covering the full  $q$  range was performed according to the work of Hammouda. In the  $\Theta$  region, a quantitative analysis of the full structure factor was done using the equivalent Kuhn chain, which enabled us to assign the  $\Theta$  region of our chain and to demonstrate, in our particular case, the failure of the Gaussian chain approach. The chain conformational properties *at the equilibrium melting temperature* are discussed using conformational distribution functions, using the largest principal component of the radius of gyration and shape parameters as order parameters. We demonstrate that for the system studied here, the Landau free energy expression based on this conformational distribution information leads to erroneous conclusions concerning the thermodynamic transition behavior. Finally, we focus on the instantaneous conformational properties *at the equilibrium melting temperature* and give a detailed analysis of the conformational shapes using different shape parameters and a simulation snapshot. We show that the chain does not only take the lamellar rod-like and globular conformational shapes, typical of the solid and liquid states, but can also explore many other conformational states, including the toroidal conformational state. It is the first demonstration that a flexible molecule like PE can also take a toroidal conformational state, which is normally linked to stiffer chains.

### Introduction

The single chain behavior is not only elementary in understanding the properties of polymers in the condensed

state but also has immediate relevance in nanoscience, nanotechnology, and experimental techniques, such as AFM, which allows for the direct study of single chains. The study of the conformational properties of a single chain by experimentation,<sup>2–19</sup> theory,<sup>20–23</sup> and simulation<sup>24–39</sup> has a long-standing history in fundamental polymer science. It is well established that a polymer chain in dilute solution can be present as an expanded coil, an ideal coil, or a

\* Corresponding author. Tel.: +32 16 327481 or +32 16 327418. Fax: +32 16 327990. E-mail: Erik.Nies@chem.kuleuven.be.

<sup>†</sup> Katholieke Universiteit Leuven.

<sup>‡</sup> Chinese Academy of Sciences.

<sup>§</sup> Eindhoven University of Technology.

collapsed globule depending on the temperature, solvent quality, and pressure.<sup>24,40,2,41–43</sup> Moreover, the expanded coil, the ideal coil, and the globule are not the only possible conformational states, and depending on the details of the intrachain and chain–solvent interactions, other conformational states may exist.<sup>44–47</sup> For instance, for stereo-regular polymers, the additional possibility exists for it to occur in the crystalline state, and the single chain can attain a folded lamellar crystalline conformational state.

Simulation and theory have contributed a great deal to the understanding of the existence of different single chain conformational states and transitions between them.<sup>24,48,49</sup> Initially, attention was given to the coil–globule transition.<sup>50,51</sup> More recently, the low temperature behavior received increased attention in computer simulation studies, and e.g., liquid–solid and solid–solid transitions have been observed.<sup>52–56</sup> The transitions between the coil, globule, and folded chain states are affected by both the environmental variables and the intrinsic character of the polymer chain. For instance, the occurrence of the globular state upon going from the expanded coil to the chain folded crystal and the length/diameter aspect ratio of the chain folded crystal sensitively depends on the chain stiffness<sup>44,57,58</sup> and the chain length.<sup>48</sup>

Unfortunately, computer simulation studies of the dense chain conformations at low temperatures are far from easy. Different instantaneous chain folded conformational states are very likely separated by high free energy barriers, making it very difficult to realize transitions from one state to the other in the time of a single Molecular Dynamics or conventional Monte Carlo simulation run. Therefore, the simulation does not necessarily represent a proper ensemble average over all relevant chain conformational states, and as a consequence, the simulation results are not necessarily representative of the behavior of real chains observed in typical experiments in which the time of the experiment is sufficiently long and/or the number of chains probed by the experiment is sufficiently large to properly sample the different conformational states. To overcome the problem of poor sampling of the rugged free energy landscape, advanced simulation methods have been developed. In particular, expanded ensemble simulation methods, such as the replica exchange method (REM) or parallel tempering (PT),<sup>59–67</sup> multicanonical ensemble method (MUCA),<sup>68–70</sup> and four dimensional expanded ensemble algorithm,<sup>71,72</sup> have proven to be very efficient.

In this work, we apply, for a polyethylene chain of finite length, canonical MD simulations combined with the replica exchange method (REMD)<sup>59,60,73</sup> to explore a wide range of temperatures, enabling us to efficiently sample the whole relevant phase space and to provide simulation data of high quality, which are representative for the equilibrium behavior of the chain molecule at all studied temperatures. From the simulation data, we obtain the radial distribution function and the structure factor of the chain as a function of the temperature and analyze these statistical properties in detail. The structure factor is the key property obtained from scattering experiments and contains statistical information on the structure of the chain molecule, and therefore this

analysis may be of use in the interpretation of such experimental data.

Subsequently, we discuss the distribution function of the largest principal component of the radius of gyration *at the equilibrium melting temperature* and discuss the applicability and the pitfalls of the use of a Landau free energy expression based on this conformational distribution information. Finally, we focus on the instantaneous conformational properties *at the equilibrium melting temperature* and give a detailed analysis of the conformational shapes using different shape parameters.

The paper is organized as follows. First the model and simulation parameters are described. Then, the structural and conformational analysis of the simulation results is presented and discussed. Finally, some conclusions are made.

## Simulation Details

In this study, a linear polyethylene chain consisting of  $N = 200$  CH<sub>2</sub> groups was modeled as a bead–spring chain using the united atom (UA) approximation for the CH<sub>2</sub> units and making no distinction between middle and end groups. The united atom approximation is widely used in the simulation of macromolecules.<sup>25,52,74,75</sup> Four types of potentials are included in our simulation, i.e., bond stretching, angle bending, torsional rotation, and van der Waals (vdW) interactions between atoms separated more than two covalent bonds along the polymer chain (i.e., including the 1–4 interaction). The potential energy expressions and the parameter values for the united atom model are taken from the DREIDING force field:<sup>76</sup>

$$U = U_{\text{bond}} + U_{\text{angle}} + U_{\text{torsion}} + U_{\text{vdw}} \quad (1)$$

in which

$$U_{\text{bond}} = \sum \frac{1}{2} K_b (l - l_0)^2,$$

$$U_{\text{angle}} = \sum \frac{1}{2} K_a (\theta - \theta_0)^2,$$

$$U_{\text{torsion}} = \sum \frac{1}{2} K_t \{1 - \cos[n(\phi - \phi_0)]\}$$

and

$$U_{\text{vdw}} = \sum \sum 4\epsilon \left[ \left( \frac{\sigma}{r} \right)^{12} - \left( \frac{\sigma}{r} \right)^6 \right]$$

(The summations denote that the potential energy terms are summed over all bonds, angles, torsion angles, and non-bonded pairs, respectively), and parameter values are given in Table S1 of the Supporting Information.

In the following, we use reduced units. The van der Waals diameter  $\sigma$ , the energy parameter  $\epsilon$ , and the mass of the united atom are taken to define reduced units that are denoted by the superscript asterisk, for example, reduced temperature  $T^* = k_B T / \epsilon$ , reduced density  $\rho^* = \rho \sigma^3$ , reduced time  $t^* = t \sqrt{(\epsilon/m)/\sigma}$ , reduced distance  $r^* = r/\sigma$ , and reduced amplitude of the scattering vector  $q^* = q\sigma$ . For the particular parameter values used in this study, the following conversions are obtained:  $t = 1.488 \times t^*$  with the time  $t$  in picoseconds and  $T = 99.921 \times T^*$  with the temperature  $T$  in degrees Kelvin.

A REMD or parallel tempering molecular dynamics (PTMD) simulation with in total 77 temperatures, covering a wide temperature range from 252 to 1511 K, was executed using at each temperature a massive Nose–Hoover chain (MNHC) thermostat.<sup>77</sup> The reduced time step was  $\Delta t^* = 1.6427 \times 10^{-3}$  (or 2.444 fs in real units). Methods to optimize the REM parameters (such as the number of replicas or the temperature distribution) have been discussed recently by Trebst et al.,<sup>78</sup> Katzgraber et al.,<sup>79</sup> Nadler and Hansmann,<sup>80–82</sup> and others.<sup>83–85</sup> In these studies, fine-tuned parameter sets and optimization strategies have been demonstrated to be useful in improving the efficiency of REM simulation. In the present work, we did not use sophisticated optimization methods. Instead, the temperatures were determined in preliminary trial REMD simulation runs, ensuring that the potential energy probability density functions (PDF) for any two adjacent temperatures have considerable overlap, such that sufficiently high swapping rates between temperatures are achieved.<sup>86</sup> The used set of reduced temperature values are given in Table S2 of the Supporting Information.

In the Supporting Information, we make a safe (conservative) estimate of the number of independent conformations contributing to the simulation results. Typically, we find that at each temperature more than 1000 truly independent conformations contribute to the simulation averages determined over large number of snapshots, typically  $10^7$  in total. More details about the parameters, the performance, and the statistics of the REMD simulation are also discussed in the Supporting Information.

## Results and Discussion

**1. Temperature Dependence of the Radial Distribution Function (RDF).** In this work, the radial distribution function (RDF) is used to investigate the intramolecular structure of the single chain. In Figure 1a and b, the equilibrium RDF is presented at different temperatures; in Figure 1a, a 3D plot is given at all simulated temperatures.

The first and highest peak in the RDF is due to the bond length distribution and appears for all temperatures at  $r^* \cong 0.422$ . The maximum of the second peak, situated at  $r^* \cong 0.690$  at the lowest temperature and slightly shifted to  $r^* \cong 0.706$  at higher temperatures, is due to the distance between 1–3 atoms (two atoms bonding to a common atom) and is close to the value  $r_{13}^* \cong 0.689$ , calculated from the Dreiding force field parameters. The shift of this peak indicates that the equilibrium bond angle in the polymer chain increases slightly as the temperature increases. The maximum of the third peak located at  $r^* \cong 1.06$  at  $T^* \cong 2.52$  shifts to a smaller value  $r^* \cong 1.04$  at the highest temperature  $T^* = 15.12$ . At the high temperatures, this peak also gets a shoulder at shorter distances. The reduced distances between 1–4 atoms (two atoms separated by three consecutive bonds along the chain) in the *trans* and the *gauche* conformations calculated from the force field are ca. 1.063 and 0.808, respectively. The *trans* state is energetically more favorable than the *gauche* state and, hence, more probable at lower temperatures. At higher temperatures, the *gauche* state becomes more populated and gives rise to the shoulder at a slightly shorter distance in the RDF. Next to the first three peaks, in Figure 1b, there are more peaks appearing at larger distances

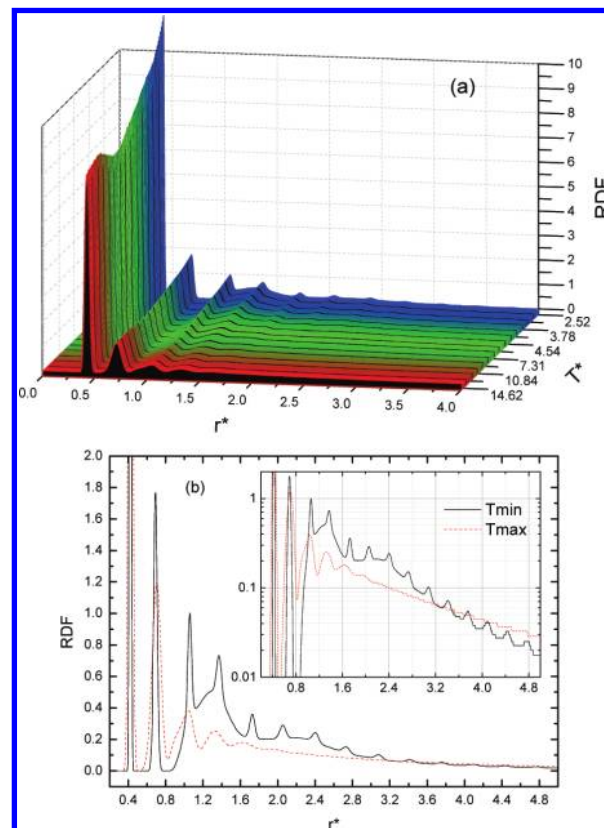


**Figure 1.** Radial distribution function of the PE chain. (a) Plot of RDF versus  $r^*$  and reduced  $T^*$ . (b) Detail of the RDF vs  $r^*$  at the lowest temperature ( $T_{\min}^* = 2.52$ ) and the highest temperature ( $T_{\max}^* = 15.12$ ).

which are well developed at the lowest temperature  $T^* = 2.52$ . The maxima of these regularly spaced peaks correspond to distances between two atoms separated by four or more consecutive bonds with all dihedral angles in the *trans* state. At low temperatures, the chain is in the folded lamellar state,<sup>86</sup> and the sharpening of these regularly spaced peaks at lower temperatures indicates the growing and perfecting of the *all-trans* stems in the chain folded structure. In an *all-trans* stem, all of the torsion angles formed by at least four consecutive chain units fall in the angular ranges  $[-\pi, -5\pi/6]$  or  $(5\pi/6, \pi]$ . The smearing out of the peaks with increasing temperature indicates the shortening and disordering of the *all-trans* stems accompanying the melting of the lamellar crystal, as discussed previously.<sup>86</sup> In Figure 1b, the RDFs at the lowest ( $T^* = 2.52$ ) and the highest ( $T^* = 15.12$ ) temperatures are compared. Here, it is noticeable that the sharp *all-trans* peaks are superimposed on a broader underlying peak.

To better understand the origin of the broadened peak in the RDF in Figure 1b, we calculate a modified RDF in which we systematically exclude more and more pair distances from the calculation. In Figure 2a and b, we show the RDFs calculated at  $T^* = 2.52$  and  $T^* = 15.12$ , respectively, with an increasing number of excluded pair distances. For example, in Figure 2, from bottom to top, curve 1 is the full RDF at the corresponding temperature, curve 2 is calculated with all pairs  $[i, i + 1]$  excluded, curve 3 is calculated with all pairs  $[i, i + 1]$  and  $[i, i + 2]$  excluded, and so on, until in curve 10, the pairs  $[i, i + 1]$ ,  $[i, i + 2]$ , ...,  $[i, i + 8]$ ,  $[i, i + 9]$  are excluded. In this way, we can hide the contributions of



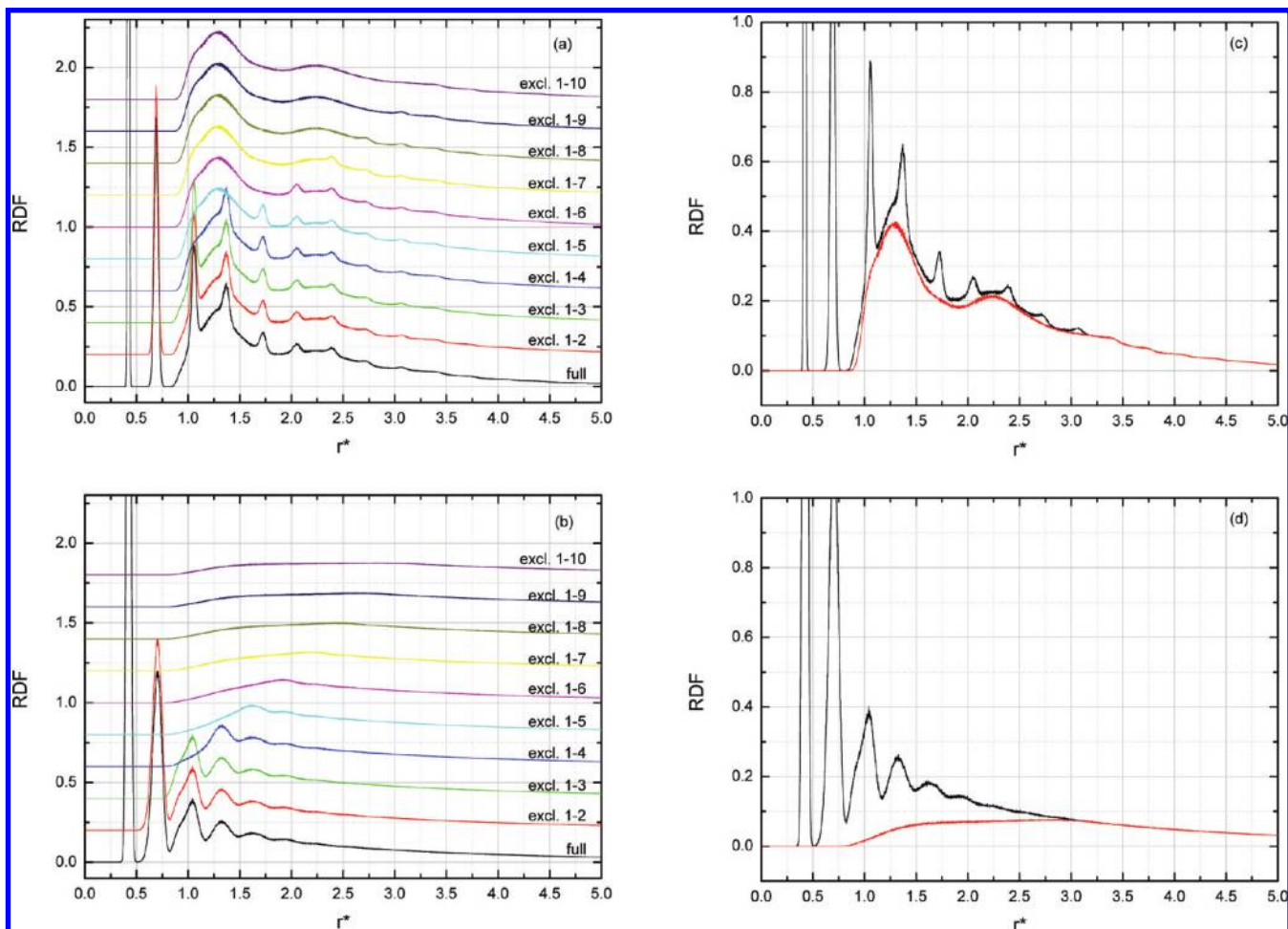
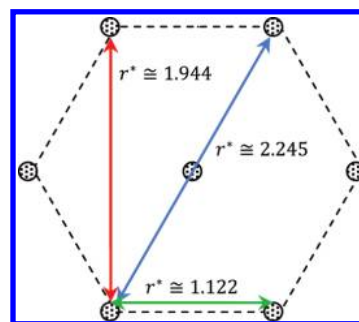


**Figure 2.** Full RDFs and partial RDFs including only nonbonded pairs that are at least separated by  $n$  number of consecutive bonds along the chain with  $n$  from 1 to 9 at the lowest temperature ( $T_{\min}^* = 2.52$ ) and the highest temperature ( $T_{\max}^* = 15.12$ ). (a) A stack plot showing the full RDF and partial RDFs with all of the exclusions at  $T_{\min}^* = 2.52$ . (b) A stack plot showing the full RDF and partial RDFs with all of the exclusions at  $T_{\max}^* = 15.12$ . (c) Comparison of the full RDF and the partial RDF with the maximal exclusion at  $T_{\min}^* = 2.52$ . (d) Comparison of the full RDF and the partial RDF with the maximal exclusion at  $T_{\max}^* = 15.12$ .

specific pair distances to the total RDF. As expected with an increasing number of excluded pair distances, the sharp peaks in the full RDF are removed, and we are left with the RDF due to pair distances farther apart along the contour of the chain. In Figure 2c and d, the full RDF and the RDF excluding all pairs up to  $[i, i + 9]$  are presented in one plot for  $T^* = 2.52$  and  $T^* = 15.12$ . The main finding here is that the nonbonded RDFs are very different for the two temperatures. At low temperatures, the nonbonded RDF clearly shows two peaks, whereas at the high temperature RDF, only one very broad smeared peak remains. At  $T^* = 2.52$ , the two rounded peaks at  $r^* \cong 1.297$  and  $r^* \cong 2.235$  are dominated by  $\text{CH}_2$  units far apart along the chain contour but that are nearest neighboring and next-nearest neighboring  $\text{CH}_2$  units in the hexagonal lamellar folded crystal. Scheme 1 gives a schematic of the cross-section perpendicular to the stems in the chain folded crystal, illustrating the hexagonal packing of the  $\text{CH}_2$  units (represented by the shaded dots). The reduced distances between the nearest ( $r^* \cong 1.122$ ) and next nearest neighboring ( $r^* \cong 1.944$  and  $r^* \cong 2.245$ )  $\text{CH}_2$  units presented in Scheme 1 are calculated from the force field parameters assuming perfect hexagonal packing of

**Scheme 1.** Schematic Cross-Section Perpendicular to the Stems in the Chain Folded Crystal, Illustrating the Hexagonal Packing of the  $\text{CH}_2$  Units in the *All-trans* Stems<sup>a</sup>



<sup>a</sup> The reduced distances between the nearest ( $r^* \cong 1.122$ ) and next nearest neighboring ( $r^* \cong 1.944$  and  $r^* \cong 2.245$ )  $\text{CH}_2$  units are calculated from the force field parameters assuming perfect hexagonal packing of stems.

stems. In Figure 2c, a clear shoulder around  $r^* \cong 1.1$  can be seen in the first underlying peak with a maximum at  $r^* \cong 1.297$ . The shoulder stems from  $\text{CH}_2$  units at the vdW nearest neighbor distance expected from the pair potential.

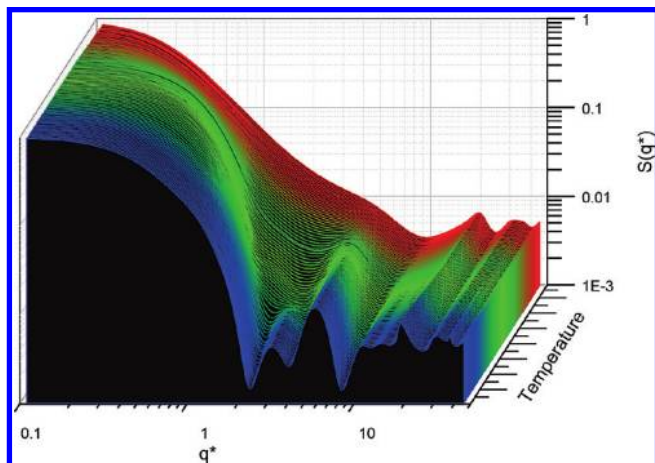


**Figure 3.** The static structure factor  $S(q^*)$  as a function of reduced  $q^*$  at the 77 simulation temperatures ranging from  $T_{\min}^* = 2.52$  to  $T_{\max}^* = 15.12$ .

However, the maximum of the peak is at  $r^* \cong 1.297$ , indicating that other distances of nonbonded pairs also contribute to this peak. The chain connectivity leads in the crystalline state to a tilting of stems,  $\text{CH}_2$  units in folds, etc. and makes it so that not all nearest neighbors are located at the most optimal vdW distance. The peak observed at  $r^* \cong 2.235$  is attributed to next nearest neighbors and contains  $\text{CH}_2$  units present in the second neighbor shell ( $r^* \cong 1.944$ ) and is attributed to first shell  $\text{CH}_2$  units in diagonal positions compared to the central  $\text{CH}_2$  unit ( $r^* \cong 2.245$ ).

In Figure 2d, at the highest temperatures  $T^* = 15.12$ , the chain is in the expanded coil state and the RDF shows a very broad peak which is characteristic for the gaseous-like density and distribution of the nonbonded pairs.

**2. Temperature Dependence of the Static Structure Factor  $S(q^*)$ .** The single-chain static structure factor for an isotropic system is defined as

$$S(q^*) = \frac{1}{N^2} \left\langle \sum_{i=1}^N \sum_{j=1}^N \frac{\sin(q^* R_{ij}^*)}{q^* R_{ij}^*} \right\rangle \quad (2)$$

where the brackets represent the time average in the MD simulation. In Figure 3,  $S(q^*)$  patterns at all temperatures used in the REMD simulation are presented in a 3D plot. We will analyze and discuss the relevant regimes of  $S(q^*)$  in detail and relate them to the structural changes with the temperature occurring in the chain.

The two shortest length scales in real space are the distances between adjacent  $\text{CH}_2$  units (the covalent bond length  $l_0^* = 0.422$ ) and the distance between two units connected to a common  $\text{CH}_2$  unit (the distance related to the bond angle  $r_0^* \cong 0.689$ ), corresponding in  $q^*$  space to  $q^* = 2\pi/l_0^* \cong 14.9$  and  $q^* = 2\pi/r_0^* \cong 9.12$ . We have ascertained that the detailed shape of  $S(q^*)$  in the large  $q^*$  regime, viz.,  $q^* > 2\pi/0.689 \cong 9.12$ , is primarily determined by the bond length and bond angle distances, which vary little with the temperature, as can be confirmed in Figure 3.

In the range  $2\pi/\sqrt{\langle R_g^2 \rangle} < q^* < 9.12$ , both local and larger scale structure information and scaling behavior for different chain states are contained. As the temperature decreases, in this  $q^*$  range, two peaks emerge (see Figure 3) which, at

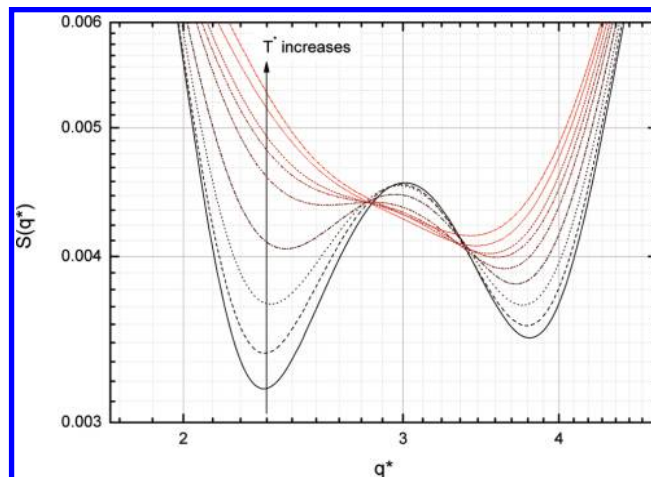


**Figure 4.**  $S(q^*)$  around  $q^* \cong 3.189$  at temperatures  $T^* = 4.083, 4.133, 4.183, 4.234, 4.284, 4.335, 4.385, 4.435$ , and  $4.486$  (corresponding to the curves from bottom to top at  $q^* = 2.3$ ).

the lowest temperature  $T^* = 2.52$ , are located at  $q^* \cong 3.189$  and  $q^* \cong 5.816$ . The corresponding distances in real space using Bragg's law are  $r^* \cong 1.970$  and  $r^* \cong 1.080$ , respectively. These distances are close to the values calculated on the basis of the force field parameters for the next nearest and the nearest neighboring *all-trans* stems (see Scheme 1). The peak at  $q^* \cong 5.816$  is related to the nearest nonbonded pairs and is present in the crystalline as well as the globular state and is characteristic of the high segmental density in these two states. In the expanded coil state, this peak disappears as the distribution of the chain segments is more typical of a gaseous state. The peak at  $q^* \cong 3.189$  corresponding to next nearest neighboring distances is only present in the crystalline state and is representative of the ordered state. The appearance of this peak can be used to determine the equilibrium melting temperature. The *equilibrium melting temperature* and the *equilibrium lamellar thickness* of the chain folded lamellar crystals have been determined previously for a PE chain with the same chain length, using the same force field. The equilibrium melting temperature was estimated from different properties: in particular, the peak position of the total heat capacity as well as the heat capacities due to van der Waals and torsional interactions were related to the solid–liquid equilibrium; the changes of the radius of gyration and of the orientational order parameters of the *all-trans* stems with temperature were used to estimate the equilibrium melting temperature.<sup>86</sup> The estimates of the equilibrium melting temperature from these different properties all gave the same value for the equilibrium melting temperature (in reduced units,  $T_m^{0*} = 4.234$ ).

In Figure 4, we show a detail of  $S(q^*)$  around  $q^* \cong 3.189$  (peak position for  $T_{\min}^* = 2.52$ ) in the vicinity of the equilibrium melting temperature. We see that a peak exists at lower temperatures with its maximum at  $q^* \approx 3$  slightly shifting to lower  $q^*$  as the temperature increases. The  $S(q^*)$  peak height at  $q^* \approx 3$  increases rapidly in the vicinity of  $T_m^{0*}$ , indicating that at this temperature the second nearest neighboring order, characteristic of the crystalline state, rapidly changes at the equilibrium melting temperature. Hence,  $S(q^*)$  can also be used to determine the equilibrium

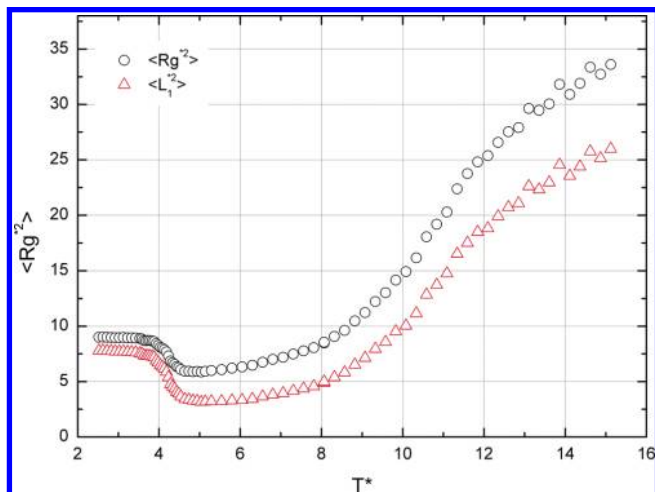


**Figure 5.** Mean squared radius of gyration  $\langle Rg^{*2} \rangle$  (circles) and largest principal component of the radius of gyration  $\langle L_1^{*2} \rangle$  (triangles).

melting temperature, leading to an estimate for  $T_m^{0*}$  in agreement with the estimate for  $T_m^{0*}$  obtained from other independent methods.<sup>86</sup>

**3. Scaling Behavior of  $S(q^*)$ .** In Figure 5, the temperature dependence of  $\langle Rg^{*2} \rangle$  and the largest principal component of the radius of gyration  $\langle L_1^{*2} \rangle$  calculated from the simulation data is shown; the details have been discussed elsewhere.<sup>86</sup>

In Figure 6a–d, the  $S(q^*)$  curves are presented at five selected temperatures, namely,  $T^* = 2.52, 5.04, 10.84, 12.60$ , and  $15.12$ .

At the lowest temperature  $T^* = 2.52$  and the highest temperature  $T^* = 15.12$  used in the REMD simulation, the chain is in the folded chain and the expanded coil state, respectively. In Figure 5, at  $T^* = 5.04$ , the chain has the smallest  $\langle Rg^{*2} \rangle$ , and at  $T^* = 10.84$ ,  $\langle Rg^{*2} \rangle$  shows an inflection point, which is an indication of the transition between the globule and coil states, although it does not define the exact  $\Theta$  state.<sup>87</sup> Finally,  $T^* = 12.60$  is selected because there is a linear part in the  $S(q^*)$  where it has a slope of  $-2$ , characteristic of ideal coil behavior.

In the Porod regime,  $q^* > 2\pi/\sqrt{\langle Rg^{*2} \rangle}$ , the structure factor may show scaling behavior,  $S(q^*) \sim (q^*)^{-\alpha}$  with  $\alpha$  the Porod exponent. The value of  $\alpha$  can be linked to the shape or the fractal character of a polymer chain. In a log–log plot of  $S(q^*)$  versus  $q^*$ , the scaling behavior becomes clear as a linear region of  $S(q^*)$  with a slope of  $-\alpha$ .

In a recent study, Hammouda presented a new Porod-like analysis to interpret the structure factor obtained in scattering experiments and applied it to small-angle neutron scattering data of polymers in a solution forming micelles of various shapes, including the sphere, the cylinder, and the lamella. His analysis shows that for a cylindrical micelle three scaling regimes exist with  $\alpha = 0, 1$ , and  $4$ . It is known that for three-dimensional objects with smooth surfaces, the Porod exponent  $\alpha = 4$ , whereas for a one-dimensional rigid rod, it should be  $1$ .<sup>1,88</sup> At the lowest temperature ( $T^* = 2.52$ ), the chain folds into a cylinder-like shape with rough surfaces and  $S(q^*)$  is flat ( $\alpha = 0$ ) at very small  $q^*$ ; at intermediate  $q^*$  values ( $0.1 < q^* < 0.2$ ),  $S(q^*) \sim (q^*)^{-1}$  can be observed. As  $q^*$  further increases, an  $\alpha = 4$  scaling is reached.

Following Hammouda, this behavior indicates that at this temperature the chain is present as a cylinder with finite thickness. When  $T^* = 5.04$ ,  $\langle Rg^{*2} \rangle$  has the smallest value; the chain is in a disordered but compact globular state. The  $S(q^*)$  (Figure 5a) shows an extended flat region at low  $q^*$  and then quickly drops with exponent  $\alpha = 4$  and can be seen to reflect that the chain is spherical with a relative smooth surface formed.<sup>1</sup> At the highest simulation temperature  $T^* = 15.12$ , see Figure 5b, the  $S(q^*)$  data follow a scaling law with  $\alpha \approx 5/3$  approximately, which indicates that the chain behaves like an excluded volume coiled chain.<sup>88</sup> At  $T^* = 12.60$ , see Figure 5b, the  $S(q^*)$  data follow scaling behavior  $S(q^*) \sim q^{*-2}$  ( $\alpha = 2$ ), which indicates the chain behaves like an ideal coil; i.e., the chain is in the  $\Theta$  state.<sup>88</sup>

**4.  $S(q^*)$  in the  $\Theta$  Region.** In Figure 7, we investigate the  $\Theta$  behavior in some more detail and compare the structure factor  $S(q^*)$  at five temperatures from the simulation results with the structure factor calculated assuming that the chain behaves like an ideal Kuhn chain.

The structure factor of the Kuhn chain is given by

$$S(x^*) = \frac{1 + (N_K - 1)(1 - x^{*2}) - 2x^*(1 + x^* + x^{*N_K})}{N_K^2(1 - x^*)^2}$$

with  $x^* = (\sin q^* l_K^*)/(q^* l_K^*)$ ,  $N_K$  being the number of Kuhn segments, and  $l_K$  being the Kuhn length.

The number of Kuhn segments, and the Kuhn length, are calculated from the end-to-end distance of the chain  $\langle R^2 \rangle$  and the contour length  $L = (N - 1) \cdot \langle l_b \rangle \cdot \sin(\langle \theta \rangle / 2)$ , with  $\langle l_b \rangle$  the effective bond length and  $\langle \theta \rangle$  the effective bond angle also obtained in the simulation. Figure 7a shows  $S(q^*) \cdot q^{*2}$  versus  $q$  (Kratky plot), and the best agreement between the simulation and the Kuhn chain results is obtained for the temperatures  $T^* = 12.60$  and  $T^* = 12.85$ . For higher and lower temperatures, the simulation data and the Kuhn result deviate significantly: the chain behaves at higher temperatures as an excluded volume chain and at lower temperatures behaves as a globule. Only at the temperatures  $T^* = 12.60$  and  $T^* = 12.85$  can the chain be treated as an ideal Kuhn chain of finite size: the temperature region  $T^* = 12.60$ – $12.85$  provides a first estimate for the  $\Theta$  region of our chain.

In Figure 7b,  $S(q^*)$  from the REMD simulation at  $T^* = 12.60$ ,  $S(q^*)$  calculated from the Debye expression for the Gaussian chain, and  $S(q^*)$  of the equivalent freely jointed Kuhn chain are compared. For the Gaussian chain, the Debye result is

$$S(Q^*) = \frac{2(e^{-Q^*} - 1 + Q^*)}{Q^{*2}}$$

with

$$Q^* = \frac{q^{*2} N l_0^{*2}}{6} = q^{*2} \langle R_g^{*2} \rangle$$

Clearly for the temperatures in the  $\Theta$  region, ideal chain behavior is reached with the appropriate scaling behavior  $S(q^*) \sim q^{*-2}$  (denoted by the dotted straight line in Figure



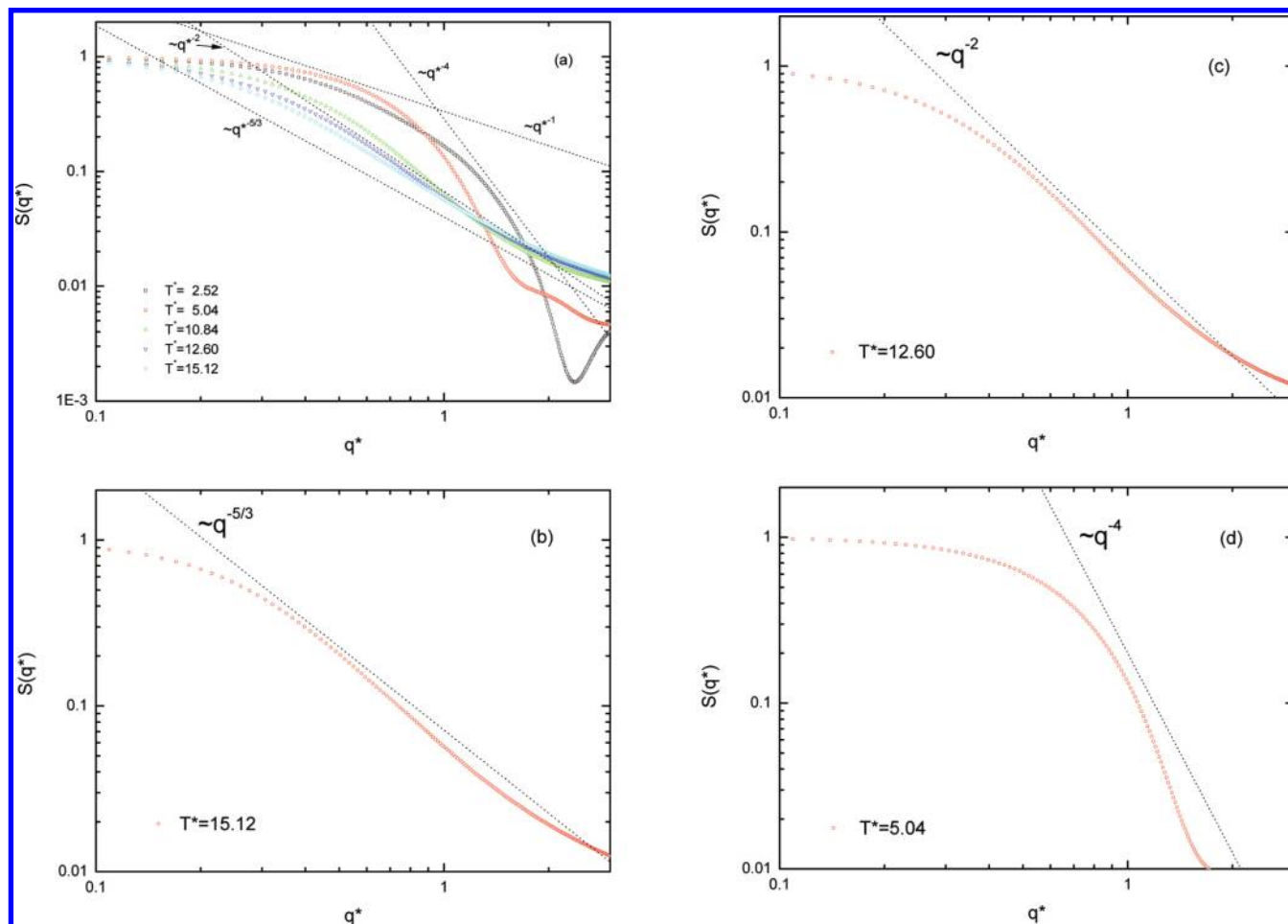


**Figure 6.** (a) Structure factor  $S(q^*)$  (shown in symbols) at five different temperatures  $T^* = 2.52$  (squares), 5.04 (circles), 10.84 (upward triangles), 12.60 (downward triangles), and 15.12 (diamonds). Relevant scaling laws (dotted straight lines) are also presented. (b) Plot of  $S(q^*)$  at  $T^* = 15.12$ . (c) Plot of  $S(q^*)$  at  $T^* = 12.60$  and (d) plot of  $S(q^*)$  at  $T^* = 5.04$ .

7b). In the small  $q^*$  range ( $q^* < 0.5$ ), the simulated  $S(q^*)$  is in good agreement with the calculated  $S(q^*)$  based on the two models. However, in the larger  $q^*$  region ( $0.5 < q^* \leq 2$ ), the simulated  $S(q^*)$  starts deviating from  $S(q^*)$  for the Gaussian chain, whereas the  $S(q^*)$  based on the Kuhn chain is still in quantitative agreement with the simulation data. This demonstrates that the ideal behavior of a real chain of finite length considered here is better described by the finite freely jointed chain than by the Gaussian chain model.

In experimental practice, Kratky plots are routinely used to determine the  $\Theta$  state in the following way: Ideal chain behavior is assumed when in the Kratky plot  $S(q^*) \cdot q^{*2}$  versus  $q^*$  becomes independent of  $q^*$  at intermediate  $q^*$ . A detailed Monte Carlo simulation study of the single chain structure factor at all length scales has been presented for sufficiently long chains under good and  $\Theta$  solvent conditions.<sup>89</sup> These authors discussed in detail the scaling behavior from a (modified) Kratky plot under good and  $\Theta$ -solvent conditions. It was clearly shown that for sufficiently long chains the (modified) Kratky plot indeed displays, in agreement with experimental practice, a plateau at intermediate  $q^*$  indicative of the chain scaling behavior. The chain length discussed in this work is certainly not long enough, and therefore the standard method of analysis does not apply. In our simulation results, we see that in the  $\Theta$  region the Kratky

plot does not show a  $q^*$  range where  $S(q^*) \cdot q^{*2}$  is independent of  $q^*$ . The reason is the following:  $S(q^*) \cdot q^{*2}$  versus  $q^*$  only has a horizontal for finite length Gaussian chains or for sufficiently long ideal chains with constant bond lengths. The number of Kuhn segments in our chain is rather small,  $N_K = 28-30$ , and therefore the necessary condition of sufficiently long chains is not met and the Kratky plot of the ideal Kuhn chain does not have a horizontal line segment. Hence, in order to ascertain whether the chain behaves ideally, it is not sufficient to search for a straight line piece; one must also take into account the long chain condition or, for smaller chains, consider the full structure factor in the range  $0 \leq q^* < l_K$ . In fact, when we use only the criterion of a horizontal line piece in the Kratky representation for our simulation data, we would conclude that at  $T^* = 13.86$  the  $\Theta$  state is reached, a considerably higher temperature than the  $\Theta$  temperature derived from scaling and the Kuhn analysis. Therefore, in the interpretation of simulation as well as experimental data, one must take care that all assumptions are obeyed in order to correctly establish ideal chain behavior.<sup>87</sup>

**5. Landau Free Energy at  $T_m^0$ : Potential Energy and Radius of Gyration Distribution Functions.** It has been reported that a chain molecule can have many different conformational states, such as coiled, globular, rod-like, and

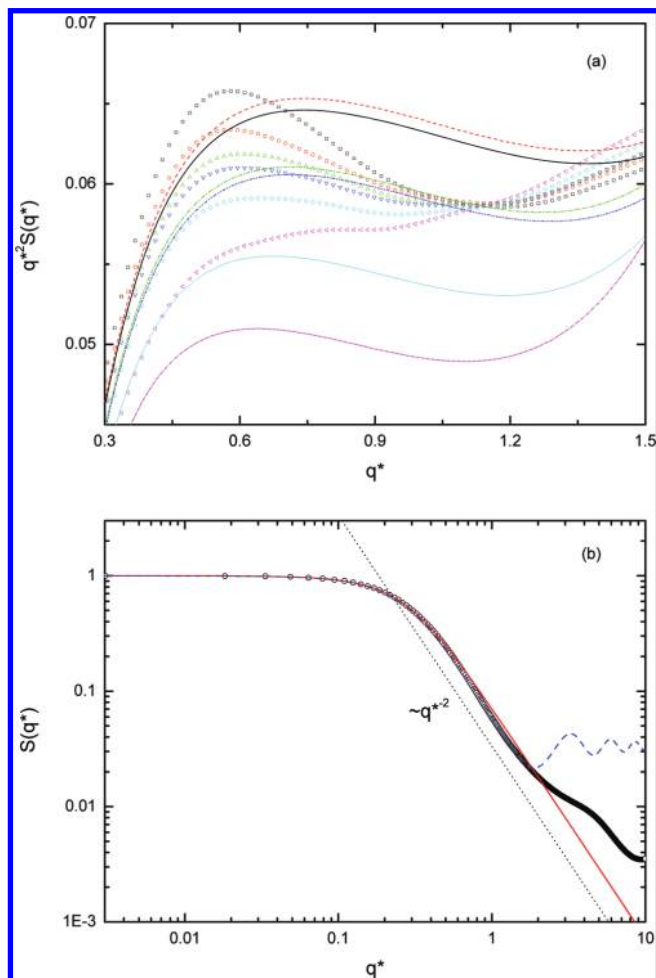


**Figure 7.** (a) Krakty plots for  $T^* = 12.10$  (squares), 12.35 (circles), 12.60 (upward triangles), 12.85 (downward triangles), 13.10 (diamonds), 13.86 (leftward triangles), together with the calculated lines based on the Kuhn model for  $T^* = 12.10$  (solid), 12.35 (dash), 12.60 (dot), 12.85 (dash dot), 13.10 (dash dot dot) 13.86 (short dash).  $T^* = 12.60$  and 12.85 show the best fitting to the calculated curve (in a sense of nonlinear least-squares fitting). (b) Comparison of the  $S(q^*)$  of the REMD simulation at  $T^* = 12.60$  (circles) and calculated  $S(q^*)$  based on the Debye formula for a Gaussian chain (solid line) and the Kuhn equivalent chain (dashed line).

toriodal states, depending on, e.g., the chain stiffness.<sup>90–100</sup> From computer simulations of a single PE chain, it is also well established that the chain can exist in the coiled, globular, and chain folded states, but whether other conformational shapes are possible and present is not clear. Here, we study the conformational shapes of the PE chain at its equilibrium melting temperature  $T_m^{0*}$  in more detail.

Figure 8 shows the probability density distribution of the potential energy, a unimodal and Gaussian-like curve.<sup>86</sup> However, when we study the relationship between the energy and the chain shapes, interesting results are found. In Figure 8b, the correlation between the potential energy and the largest principal component of the mean squared radius of gyration  $L_1^{*2}$  at  $T_m^{0*} = 4.23$  is presented in a scatter plot. Each point in the scatter plot represents one chain configuration found in the equilibrium trajectory, which contains  $5 \times 10^5$  configurations in total.

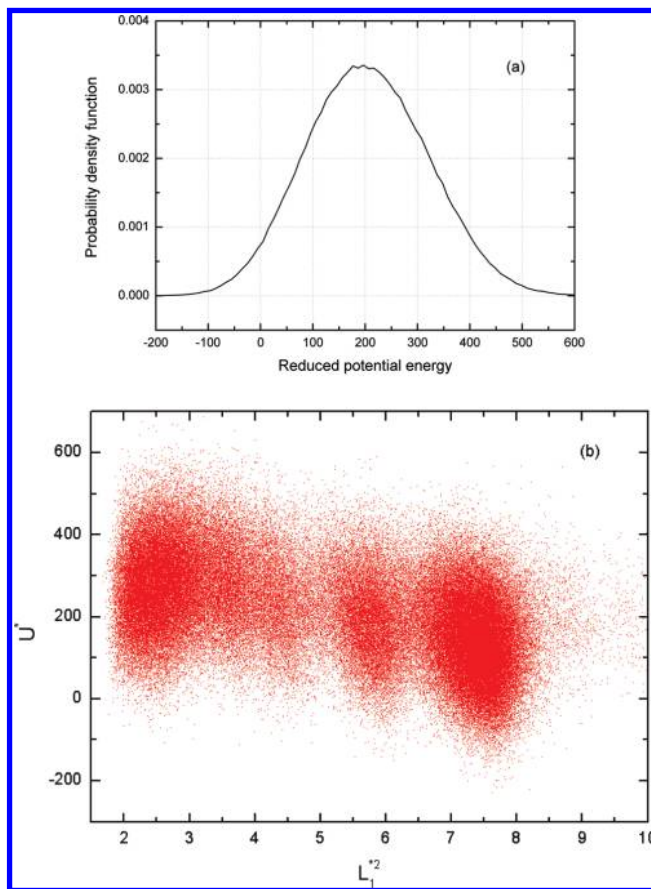


**Figure 8.** (a) Probability density distribution of the reduced potential energy and (b) correlation between the reduced potential energies  $U^*$  and the largest principal component of radius of gyration  $L_1^{*2}$  of  $5 \times 10^5$  chain configurations at the crystallization temperature  $T_m^{0*} = 4.23$ . (b) It is clearly shown that the population of conformations is unevenly and broadly distributed along  $L_1^{*2}$ , implying that the chain configurations can be divided into several groups on the basis of a structural parameter such as  $L_1^{*2}$ .

The probability density function (PDF) of  $L_1^{*2}$ , denoted by  $P(L_1^{*2})$ , is presented in Figure 9a. The multimodal feature in  $P(L_1^{*2})$  has also been observed in the radius of gyration by others.<sup>91</sup> However, the PDF of the potential energy  $P(U^*)$  is unimodal, as shown in Figure 8a. To understand how the configurations with different structural parameters contribute to the thermodynamic quantity  $U^*$ , the chain configurations around each peak found in  $P(L_1^{*2})$  are grouped by their  $L_1^{*2}$  values. Therefore, five groups are defined corresponding to the five peaks found in  $P(L_1^{*2})$  (the name and boundary for each group are labeled in Figure 9a). The chain configurations in each group are extracted, and the PDF of the potential energy for the chain configurations in each group is calculated. The PDFs for the five configuration groups ( $P_i(U^*)$ ,  $i = 1-5$ , with  $i$  the peak index; thin lines) are presented in Figure 9b. Clearly, the energy distributions  $P_i(U^*)$  for the different groups are not distinct and show considerable overlap. Peak 1 in Figure 9a, which is located at the largest  $L_1^{*2}$ , gives  $P_1(U^*)$  at the lowest energy in Figure 9b. Peak 2, which has the smallest  $L_1^{*2}$ , possesses a distribution at higher energies. The energy distributions of peaks 3 and 4 are in between the distributions of peaks 1



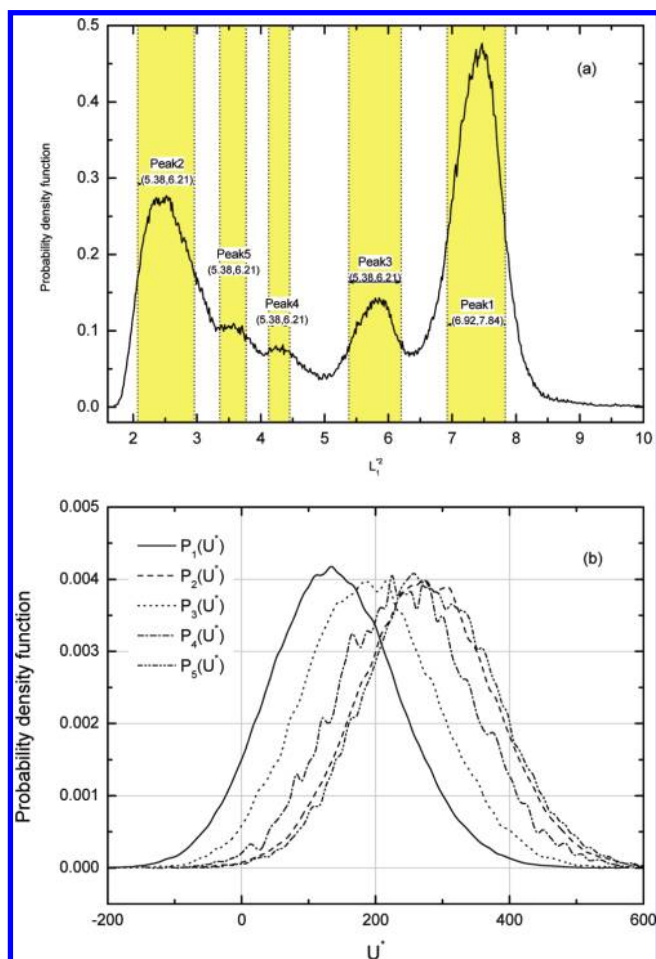


**Figure 9.** (a) Probability density function of  $L_1^{*2}$  and the definition of the configuration groups based on the peak locations. (b) The normalized energy distributions for the chain configurations in each configuration group.

and 2, with the peak with smaller  $L_1^{*2}$  having a higher energy distribution  $P_i(U^*)$ . However, peak 5 is an exception to the relationship between  $L_1^{*2}$  and  $U^*$ . It is located at higher  $L_1^{*2}$  than peak 2 but also produces an energy distribution  $P_5(U^*)$  at slightly higher energy than  $P_2(U^*)$ .

Before we show the relation between chain dimension and shape, we would like to comment on the use of a Landau free energy expression  $A_L(Q)$  in dependence on a structure parameter  $Q$ , viz.,  $A_L(Q) = A - kT \log(p_Q(Q))$ , where  $A$  is the Helmholtz free energy and  $p_Q(Q)$  the canonical probability distribution for an order parameter  $Q$ . Bimodal and multimodal probability distributions of  $R_g^{*2}$  or  $L_1^{*2}$  as have been presented before in single chain studies were used to obtain a Landau free energy expression.<sup>91,96</sup> Multi(bi)modality in  $\langle L_1^{*2} \rangle$  leads to a multi(bi)modal Landau free energy implying true thermodynamic coexistence between different conformational states. However, in our case, this conclusion is not valid, as the potential energy probability density distribution is unimodal (see Figure 8a) and not multi- or bimodal. Only when there is a one-to-one correspondence between the energies of the different conformational states and the structure parameter  $Q$  (e.g.,  $R_g^{*2}$  or  $L_1^{*2}$ ) characterizing the different conformational states, bi(multi)modality in the energy probability density (necessary for thermodynamic coexistence) would lead to a bi(multi)modality in the

conformational parameter that could be correctly interpreted in terms of thermodynamic coexistence. Hence, the bi- or multimodality in  $\langle L_1^{*2} \rangle$  or  $\langle R_g^{*2} \rangle$  observed here does not mean true coexistence as in a first order phase transition. As discussed before, for the case studied here, the solid–liquid transition is a continuous transition.<sup>86</sup> Therefore, the use and applicability of a Landau free energy expression requires that a unique one-to-one correspondence exists between the order parameter probability density used in the Landau free energy approach and the energy probability density relevant for thermodynamic coexistence behavior. This condition should be specifically checked to ascertain the applicability of the Landau free energy approach.

**6. Instantaneous Conformational Shapes and Shape Parameters at  $T_m^0$ .** The pattern found in Figure 8b inspired us to analyze the conformational data using shape parameters also used by Binder et al.<sup>87,101</sup> Two instantaneous shape parameters  $K_1$  and  $K_2$  are defined by

$$K_1 = \frac{L_2^{*2} + L_3^{*2}}{L_1^{*2} + L_2^{*2}}, K_2 = \frac{L_1^{*2} + L_3^{*2}}{L_1^{*2} + L_2^{*2}} \quad (3)$$

with  $L_1^{*2} \geq L_2^{*2} \geq L_3^{*2}$  being the instantaneous principal components of the radius of gyration. Note that  $K_2 \geq K_1$  and  $K_2 \geq 0.5$  are always true. As their name suggests, these shape parameters can describe many different shapes of chain molecules. For example, the polymer chain has a spherical shape when  $K_1 \rightarrow 1$  and  $K_2 \rightarrow 1$ , a thin rod conformation when  $K_1 \rightarrow 0$  and  $K_2 \rightarrow 1$ , or a thin round disk or ring-like structure when  $K_1 \rightarrow 0.5$  and  $K_2 \rightarrow 0.5$ . Other combinations of  $K_1$  and  $K_2$  represent intermediate chain shapes in between those extremes, e.g., ellipsoid.

$K_1$  and  $K_2$  for the  $5 \times 10^5$  instantaneous chain configurations are calculated, and the contour map of the resulting population as a function of the shape parameters  $K_1$  and  $K_2$  is presented in Figure 10. According to the definitions of the shape parameters,  $K_2 \geq 0.5$  and  $K_2 > K_1$ . As we can see at  $T_m^0$ , the population covers almost all of the possible combinations of  $K_1$  and  $K_2$ . This is a very interesting result, since the broad distribution in the shape parameter space implies that the chain adopts not only the globular and rod-like conformations but also very diverse shapes at the transition temperature. Furthermore, the contour map shows several highly populated regions, which suggests that some shapes are particularly more favorable. The most dense population is located at very small  $K_1$  and large  $K_2$  values, which define the rod-like structure in agreement with the folded chain lamellar shape. Another highly populated region in Figure 10a is centered at  $K_1 \approx 0.65$  and  $K_2 \approx 0.85$ , which are the values typical for ellipsoidal shapes. It is clear that this region is broader than the region of the rod-like shapes, which implies that the shapes of the individual configurations vary a lot (from more disk-like to more spherical ellipsoids). Besides these two most obvious regions, there are also some less populated but recognizable high density regions in between, as can be seen in Figure 10a and b.

With the same definition for the peaks as given in Figure 9a, chain configurations having similar  $L_1^{*2}$  are grouped together, and their shape parameters are retrieved to locate

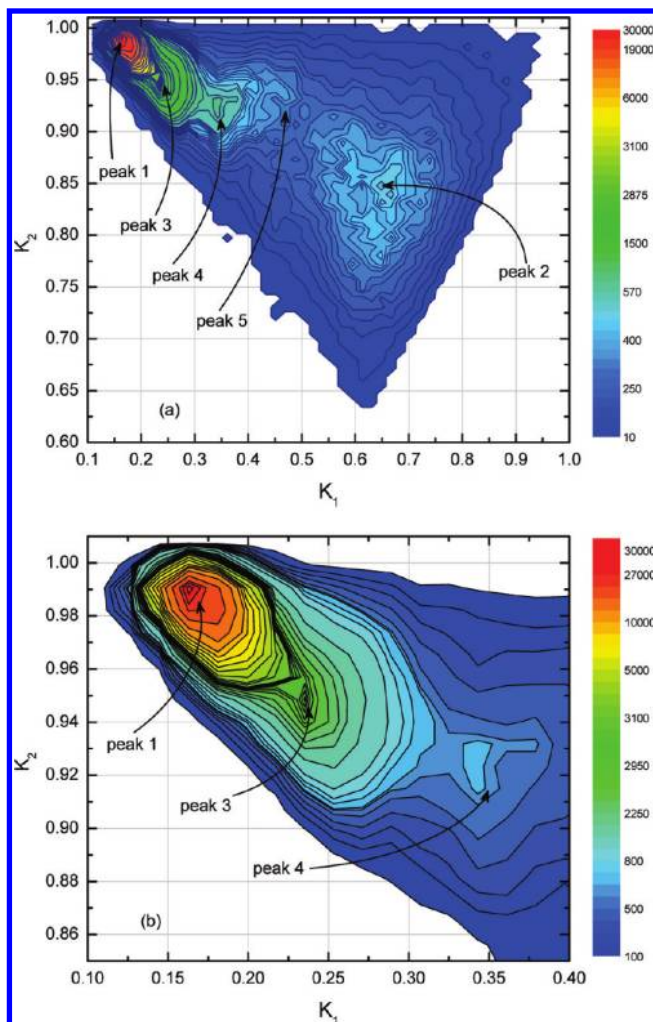


**Figure 10.** (a) Contour map of the population of the  $5 \times 10^5$  chain configurations in the 2D space defined by the shape parameters  $K_1$  and  $K_2$  at the equilibrium melting temperature  $T_m^0 \cong 4.234$  and (b) detail of the contour map in the small  $K_1$  region.

them on the shape parameter map shown in Figure 10. In Figure 10a, the five configuration groups are indicated by the arrows in the  $K_1$ – $K_2$  shape parameter map. Then, the shape parameter distributions of all the configurations and the configurations belonging to the defined groups are presented in Figure 11a and b for  $K_1$  and  $K_2$ , respectively. Along the  $K_1$  axis, the five distributions are totally separated, whereas along  $K_2$  they strongly overlap. This is due to the fact that the ratio between the largest component  $L_1^{*2}$  and two smaller components  $L_2^{*2}$  or  $L_3^{*2}$  of the radius of gyration is more prominent than the ratio between the two smaller ones  $L_2^{*2}/L_3^{*2}$ . As a result,  $K_1$  is a better measure for identifying the different individual chain shapes at the equilibrium melting temperature.  $P(K_1)$  shows obvious multiple peak features as also observed in  $P(L_1^{*2})$ .

**7. Instantaneous Shapes at  $T_m^0$ : Snapshots of Representative Chain Conformations.** The distributions of the shape parameters  $K_1$  and  $K_2$  give statistical information. From Figure 11, we know peak 1 includes chain configurations having the smallest  $K_1 \rightarrow 0$  but largest  $K_2 \rightarrow 1$ , which clearly tells us most of them are rod-shaped. Peak 2 (both small  $K_1$  and  $K_2$ ) collects conformations which are more spherical.

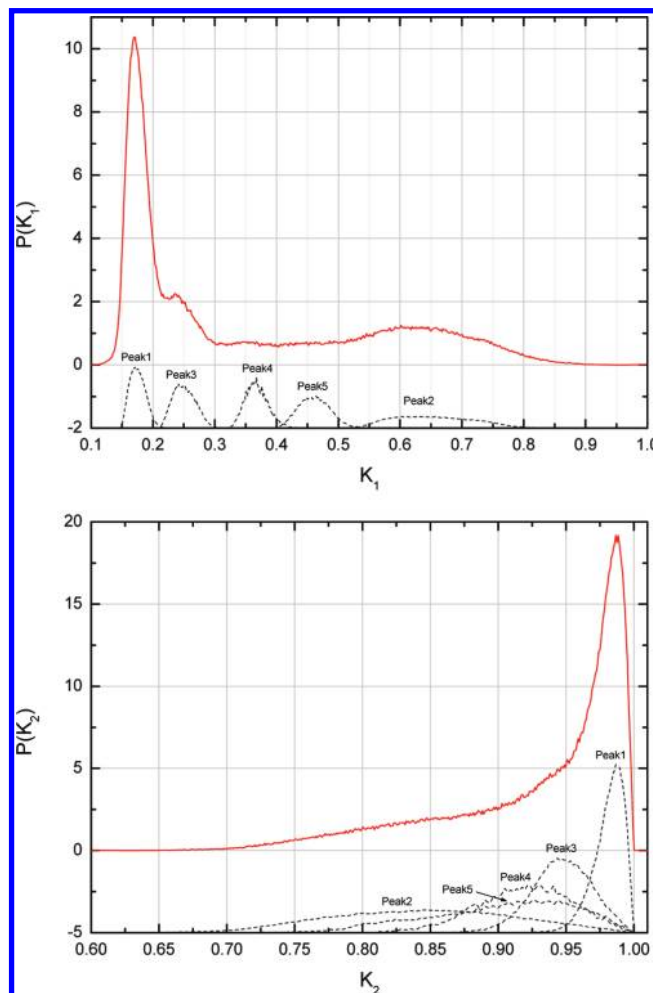


**Figure 11.** Probability density distribution of the  $5 \times 10^5$  chain configurations as a function of shape parameter  $K_1$  (a) and  $K_2$  (b) at the equilibrium melting temperature  $T_m^0 \cong 4.234$ . The normalized distributions of  $K_1$  and  $K_2$  of the chain configurations in the separate configuration groups are also presented in a and b, respectively.

Peaks 3, 4, and 5 sit in between, which means the overall shapes change from a perfect rod to ellipsoid.

Molecular simulations allow us to study individual configurations in great detail. To verify our analysis based on the shape parameters and to characterize the chain configurations in the aforementioned configuration groups, snapshots for the chain configurations in each group are extracted and visualized.

First, the extreme configuration at the smallest  $K_1 = 0.114$  and the largest  $K_2 = 0.992$  observed during the simulation is shown in Figure 12. The polymer chain folds itself into six parallel stems forming a long and thin rod. However, the parallel stems are not perfectly aligned, and this causes the  $\text{CH}_2$  units in the loops and at the ends of the parallel stems to have fewer van der Waals contacts with neighboring stems than when the stems would be properly aligned. As a consequence, the potential energy increases. This explains why this configuration does not fall into the most probable region defined by peak 1 in the shape parameter map.

The second extreme is located in the upper-right corner of the shape parameter map triangle with both  $K_1$  and  $K_2$

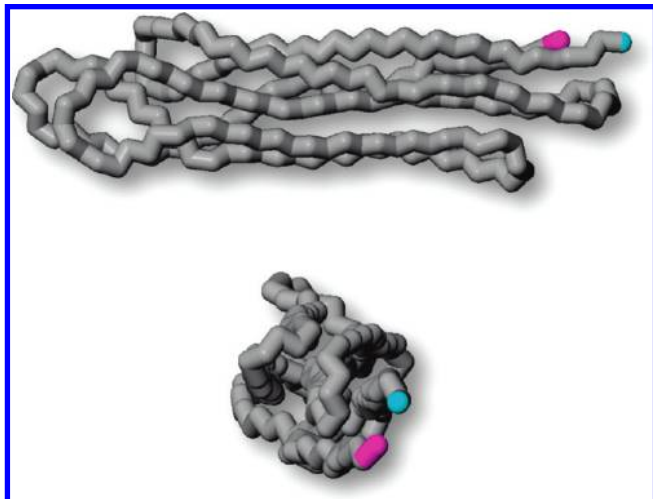


**Figure 12.** Lateral view and intersection view of the chain configuration ( $N = 200$ ) with shape parameters  $K_1 = 0.114$  and  $K_2 = 0.992$  at  $T_m^0 \cong 4.234$ .

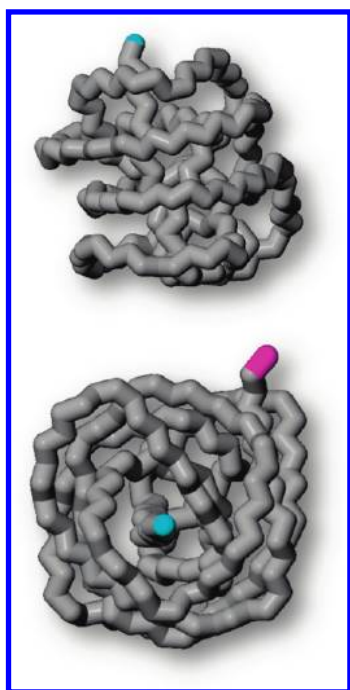


**Figure 13.** Lateral view and intersection view of the chain configuration ( $N = 200$ ) with shape parameters  $K_1 = 0.876$  and  $K_2 = 0.930$  at  $T_m^0 \cong 4.234$ .

approaching 1 ( $K_1 = K_2 = 1$  represent a perfect sphere). In our simulation, the configuration with the largest  $K_1$  and the largest  $K_2$  simultaneously is found at  $K_1 = 0.876$  and  $K_2 = 0.930$  and is shown in Figure 13. The side view and the top view show that the chain has similar sizes in all dimensions, although it is far from a perfect sphere. Furthermore, the chain shows some kind of ordering: some short *all-trans* segments swirl about one axis and keep parallel to each other.

Disk-like shapes have similar  $K_1$  and  $K_2$  values. A chain configuration having  $K_1$  and  $K_2$  the closest to each other is located at  $K_1 = 0.601$  and  $K_2 = 0.638$  and is shown in Figure 14. It looks more like a “donut” than a disk. Similar toroidal structures for a polymer chain have also been observed in other simulations<sup>24,87,96,97,99,101,102</sup> for polymer chains with

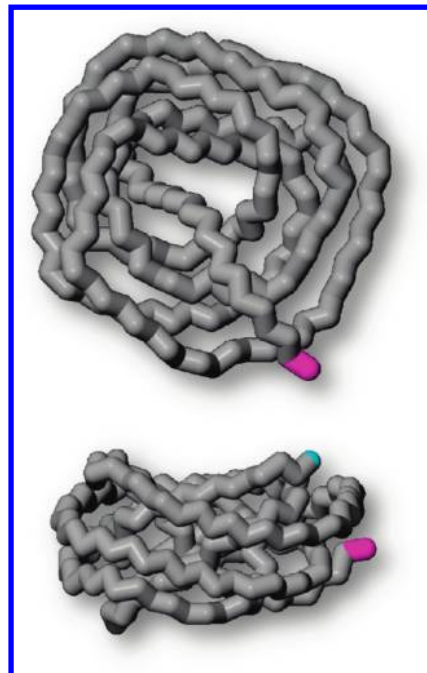


**Figure 14.** Lateral view and intersection view of the chain configuration ( $N = 200$ ) with shape parameters  $K_1 = 0.601$  and  $K_2 = 0.638$  at  $T_m^0 \cong 4.234$ .

a high degree of stiffness. Although polyethylene is normally categorized as a flexible chain, toroidal shapes can also be explored by the PE chain.

The three extreme conformations presented above do not represent the most probable conformation in each group. However, they help us to understand or imagine what an actual chain configuration looks like and the link between the shape parameters and the chain unit arrangement. To study the most probable configurations, we show in Figure 15 the snapshots of representative chain configurations located in the peak positions of the five different groups in Figure 11a and b.

Figure 15a shows a typical rod-like structure formed by parallel arranged *all-trans* stems found at  $K_1 = 0.172$  and  $K_2 = 0.987$ . Unlike the configuration shown in Figure 12, the *all-trans* stems appear to be better aligned and form a well ordered rod with both ends capped by the chain loops. There are seven folds in the rod-shaped configuration, which is less than the number found for the conformation in Figure 12, and therefore the rod is shorter. This configuration has lower energy since both the conformational energy and the nonbonded interaction are minimized.

For the other highly populated peak, peak 2, the favorable configuration at  $K_1 = 0.602$  and  $K_2 = 0.864$  looks like the one presented in Figure 15b, a compact ellipsoid with a certain degree of ordering. The configuration presented in Figure 15c is found in peak 3 (the one next to group 1 along  $K_1$ ) with  $K_1 = 0.242$  and  $K_2 = 0.944$ . It has eight folds and even shorter *all-trans* segments. It is also twisted because of the occurrence of a few defects (i.e., a few *gauche* conformations) in the stems. Figure 15d and e are the configurations at the centers of peaks 4 and 5 in the shape parameter map, respectively. These groups of intermediate  $K_1$  and  $K_2$  collect many different shapes which are located



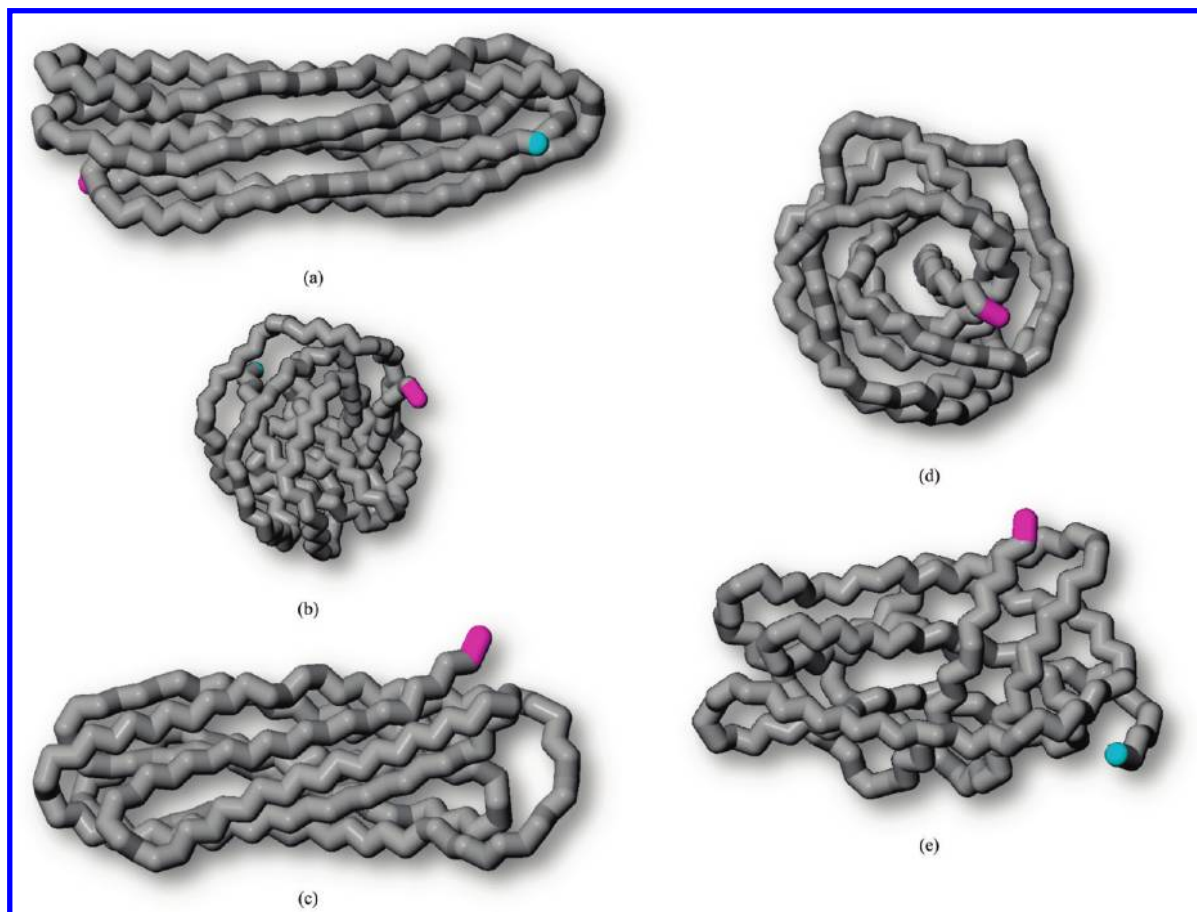


**Figure 15.** Snapshots of typical chain configurations ( $N = 200$ ) selected in the peak maxima of the shape parameter distributions shown in Figure 11. (a)  $K_1 = 0.172$  and  $K_2 = 0.987$ , (b)  $K_1 = 0.602$  and  $K_2 = 0.864$ , (c)  $K_1 = 0.242$  and  $K_2 = 0.944$ , (d)  $K_1 = 0.367$  and  $K_2 = 0.930$ , and (e)  $K_1 = 0.463$  and  $K_2 = 0.926$ .

between the perfect rod and the ellipsoid. Figure 15d presents the configuration found at  $K_1 = 0.367$  and  $K_2 = 0.930$ : it is a thicker toroid. The configuration in Figure 15e with  $K_1 = 0.463$  and  $K_2 = 0.926$  looks like an intermediate state between the folded rod and the toroidal configuration with the *all-trans* stems tilted.

## Conclusions

Using the parallel tempering canonical molecular dynamics method, a polyethylene chain of 200  $\text{CH}_2$  united atom units is simulated in a very broad temperature range covering both the coil–globule and the globule–rod transitions of the polymer chain. The structural and conformational properties of the polyethylene chain derived from the simulation results are discussed.

The radial distribution function and the structure factor of the chain have been analyzed in great detail. The peaks in the RDF have been assigned to characteristic distances in the chain: bond length, bond angle, torsional distances of four  $\text{CH}_2$  units up to 10  $\text{CH}_2$  units provide distinct and sharp peaks in the RDF which gradually broaden with increasing temperature. The peaks related to torsional distances of four and more  $\text{CH}_2$  units gradually disappear with increasing temperature. However, these peaks do not disappear abruptly at the equilibrium melting temperature, and therefore these peaks are not typical for the crystalline state or the equilib-

rium transition temperature. At the equilibrium melting temperature, a broad peak appears that becomes more pronounced at lower temperatures. This broader peak stems from next nearest neighbor hexagonal distances characteristic of the ordered crystalline lamellar state.

Also in the structure factor  $S(q^*)$ , the different peaks have been analyzed and assigned to different length scales in the chain molecule. At very high  $q^*$ ,  $S(q^*)$  is related to smaller length scales, and distinct features due to bond lengths, bond angles, and torsion angles were resolved and can serve as fingerprints for these atomistic distances in the chain. At smaller  $q^*$  values, in the regime  $[\sqrt{\langle R_g^2 \rangle}]^{-1} \ll q^* \ll l_0^{-1}$ , the structure factor reflects both local and larger-scale structure information. In this regime, two peaks emerge as the temperature decreases that are located at the lowest temperature  $T_{\min}^* = 2.52$  at  $q^* \cong 3.189$  and  $q^* \cong 5.186$ . The peak at  $q^* \cong 5.186$  is also present in the globular state and is thus not representative for the crystallized chain but is related to nearest neighbor distances which are typical for the high segment densities in the crystalline and globular states. On the other hand, the peak at  $q^* \cong 3.189$  is related to the formation of periodic structures and has successfully been used to determine the equilibrium melting temperature on the basis of structure factor (scattering) information. The use of  $S(q^*)$  in this manner links to the experimental practice of studying crystallization/melting transitions in materials

using scattering techniques, and the equilibrium melting temperature established in this way is in quantitative agreement with the equilibrium melting temperature determined from other properties.<sup>86</sup>

Following Hammouda, the full  $q^*$ -range scaling behavior of  $S(q^*)$  is studied in detail and related to the conformational properties. At low temperatures, the scaling analysis indicates that the chain is in a rod-like structure. At temperatures slightly higher than the equilibrium melting temperature, the scaling behavior is found to be in agreement with the globular state, and at the highest temperature, the scaling behavior is indicative of the expanded excluded volume coil.

In the  $\Theta$  region, the ideal chain behavior is not only shown by the scaling analysis but is also obtained from a quantitative comparison of the full  $S(q^*)$  with the structure factor of the equivalent Kuhn chain. In doing this detailed analysis, we have been able to determine the  $\Theta$  region of our chain with good accuracy without having to resort to the studies of different chain lengths.

However, we also have shown that a correct assignment of the  $\Theta$  region requires care, and the presence of a horizontal line piece in the Kratky plot is not sufficient evidence of  $\Theta$  conditions. For our PE 200 chain, the equivalent Kuhn chain only contains ca. 30 Kuhn segments, which is not long enough to fulfill the long or Gaussian chain approximations. As a result, in the Kratky plot, the ideal chain behavior is not reflected by a horizontal line piece at intermediate  $q^*$  in  $S(q^*) \cdot q^{*2}$  vs  $q^*$  (typical for Gaussian chains and in practice used as the signature of ideal chain behavior) but has a sigmoidal shape. However, at higher temperatures when the chain behaves already as an excluded volume chain, a horizontal line piece is present in the Kratky plot, and one could mistakenly take this temperature as the  $\Theta$  temperature. Therefore, for smaller chain lengths, only a comparison of the full structure factor leads to consistent and accurate determination of the  $\Theta$  region.

A detailed analysis of the chain conformational shapes was done at the equilibrium melting temperature. The conformational shapes of the PE chain were represented in conformational distribution functions using the eigenvalue of the largest principal component of the radius of gyration tensor as well as the shape parameters  $K_1$  and  $K_2$  as order parameters. The conformational distribution functions have a multimodal dependence on the selected order parameters. The different distinct conformational regions that were found include the already known expanded coil, globular, and chain folded lamellar structures. However, also a distinct region of toroidal or more disk-like structures is discernible. These structures are normally linked to stiffer chain molecules and are rather unexpected for the flexible PE molecule. So far, the toroidal state had not been identified in simulations on PE chains. From our results, it is now clear that, at the equilibrium transition temperature, the PE chain can take, next to the common rod-like lamellar and globular structures, indicative of the solid and liquid states, also a greater diversity of conformational shapes, including toroidal shapes.

Although different conformational regions are found, their potential energy probability densities are not distinct but largely overlap. As a consequence, the use of the multimodal

conformational density distributions in a Landau free energy lead to erroneous predictions of true thermodynamic coexistence behavior between different conformational states. In our case studied here, the chain conformations can continuously change from one region to the other, resulting also in a continuous transition instead of a first-order transition characterized by coexisting states. The applicability of the Landau free energy approach should always be checked and is only valid when there is a one to one correspondence between the energy and conformational distributions. The shape parameter analysis is further clarified and exemplified by a study of characteristic snapshots from the conformational distribution function.

**Acknowledgment.** The authors thank the Funds for Scientific Research Flanders for financial support. T.L. is indebted to the Katholieke Universiteit Leuven for a postdoctoral fellowship (OT 03/93). The computations for this research have been done on the VIC HPC supercomputer of the K. U. Leuven.

**Supporting Information Available:** Model description and force field parameters and information on the performance and statistics of the REMD simulation. This material is available free of charge via the Internet at <http://pubs.acs.org>.

## References

- (1) Hammouda, B. *J. Appl. Crystallogr.* **2010**, *43*, 716–719.
- (2) Xu, J.; Zhu, Z.; Luo, S.; Wu, C.; Liu, S. *Phys. Rev. Lett.* **2006**, *96*.
- (3) Wang, X.; Wu, C. *Macromolecules* **1999**, *32*, 4299–4301.
- (4) Wang, X.; Qiu, X.; Wu, C. *Macromolecules* **1998**, *31*, 2972–2976.
- (5) Wu, C.; Zhou, S. *Phys. Rev. Lett.* **1996**, *77*, 3053.
- (6) Chu, B.; Ying, Q.; Grosberg, A. Y. *Macromolecules* **1995**, *28*, 180–189.
- (7) Swislow, G.; Sun, S.; Nishio, I.; Tanaka, T. *Phys. Rev. Lett.* **1980**, *44*, 796.
- (8) Huser, T.; Yan, M.; Rothberg, L. J. *Proc. Natl. Acad. Sci. U.S.A.* **2000**, *97*, 11187–11191.
- (9) Tanaka, T. *Polymer* **1979**, *20*, 1404–1412.
- (10) Perkins, T.; Smith, D.; Chu, S. *Science* **1994**, *264*, 819–822.
- (11) Deniz, A. A.; Mukhopadhyay, S.; Lemke, E. A. *J. R. Soc. Interface* **2008**, *5*, 15–45.
- (12) Perkins, T.; Smith, D.; Larson, R.; Chu, S. *Science* **1995**, *268*, 83–87.
- (13) Kumaki, J.; Nishikawa, Y.; Hashimoto, T. *J. Am. Chem. Soc.* **1996**, *118*, 3321–3322.
- (14) Kumaki, J.; Hashimoto, T. *J. Am. Chem. Soc.* **2003**, *125*, 4907–4917.
- (15) Ortiz, C.; Hadziioannou, G. *Macromolecules* **1999**, *32*, 780–787.
- (16) Bemis, J. E.; Akhremitchev, B. B.; Walker, G. C. *Langmuir* **1999**, *15*, 2799–2805.
- (17) Rief, M.; Oesterhelt, F.; Heymann, B.; Gaub, H. E. *Science* **1997**, *275*, 1295–1297.

- (18) Zlatanova, J.; Lindsay, S. M.; Leuba, S. H. *Prog. Biophys. Mol. Biol.*, **74**, 37–61.
- (19) Fritz, J.; Anselmetti, D.; Jarchow, J.; Fernandez-Busquets, X. *J. Struct. Biol.* **1997**, *119*, 165–171.
- (20) Stockmayer, W. H. *Die Makromolekulare Chemie* **1960**, *35*, 54–74.
- (21) Mattice, W. L.; Suter, U. W. *Conformational Theory of Large Molecules: The Rotational Isomeric State Model in Macromolecular Systems*; 1st ed.; Wiley-Interscience, 1994.
- (22) Flory, P. J. *Statistical Mechanics of Chain Molecules*; Reprint.; Oxford Univ Pr (Sd), 1989.
- (23) Yamakawa, H. *Modern theory of polymer solutions*; Harper & Row, 1971.
- (24) Binder, K.; Paul, W.; Strauch, T.; Rampf, F.; Ivanov, V.; Luettmner-Strathmann, J. *J. Phys.: Condens. Matter* **2008**, *20*, 494215.
- (25) Liao, Q.; Jin, X. *J. Chem. Phys.* **1999**, *110*, 8835.
- (26) Baumgärtner, A. *J. Chem. Phys.* **1980**, *72*, 871.
- (27) Jeppesen, C.; Kremer, K. *Europhys. Lett.* **1996**, *34*, 563–568.
- (28) Hu, W. *J. Chem. Phys.* **1998**, *109*, 3686.
- (29) Wittkop, M.; Kreitmeier, S.; Göritz, D. *J. Chem. Phys.* **1996**, *104*, 3373.
- (30) Noguchi, H.; Yoshikawa, K. *J. Chem. Phys.* **1998**, *109*, 5070.
- (31) Takahashi, M.; Yoshikawa, K.; Vasilevskaya, V. V.; Khokhlov, A. R. *J. Phys. Chem. B* **1997**, *101*, 9396–9401.
- (32) Taylor, M. P.; Paul, W.; Binder, K. *J. Chem. Phys.* **2009**, *131*, 114907.
- (33) Narambuena, C.; Leiva, E.; Chávez-Páez, M.; Pérez, E. *Polymer* **2010**, *51*, 3293–3302.
- (34) Ivanov, V. A.; Stukan, M. R.; Müller, M.; Paul, W.; Binder, K. *J. Chem. Phys.* **2003**, *118*, 10333.
- (35) Stukan, M. R.; Ivanov, V. A.; Grosberg, A. Y.; Paul, W.; Binder, K. *J. Chem. Phys.* **2003**, *118*, 3392.
- (36) Kremer, K.; Binder, K. *Comput. Phys. Rep.* **1988**, *7*, 259–310.
- (37) Zhou, Y.; Hall, C. K.; Karplus, M. *Phys. Rev. Lett.* **1996**, *77*, 2822–2825.
- (38) Liang, H.; Chen, H. *J. Chem. Phys.* **2000**, *113*, 4469.
- (39) Baysal, B. M.; Karasz, F. E. *Macromol. Theory Simul.* **2003**, *12*, 627–646.
- (40) Swislow, G.; Sun, S.; Nishio, I.; Tanaka, T. *Phys. Rev. Lett.* **1980**, *44*, 796–798.
- (41) Harano, Y.; Kinoshita, M. *J. Phys.: Condens. Matter* **2006**, *18*, L107–L113.
- (42) Polson, J. M.; Moore, N. E. *J. Chem. Phys.* **2005**, *122*, 024905.
- (43) Kunugi, S.; Tada, T.; Yamazaki, Y.; Yamamoto, K.; Akashi, M. *Langmuir* **2000**, *16*, 2042–2044.
- (44) Martemyanova, J. A.; Stukan, M. R.; Ivanov, V. A.; Müller, M.; Paul, W.; Binder, K. *J. Chem. Phys.* **2005**, *122*, 174907.
- (45) Liao, Q.; Dobrynin, A. V.; Rubinstein, M. *Macromolecules* **2006**, *39*, 1920–1938.
- (46) Noguchi, H.; Yoshikawa, K. *J. Chem. Phys.* **1998**, *109*, 5070.
- (47) Berghmans, H.; Deberdt, F. *Philos. Trans. R. Soc. Lond., Ser. A* **1994**, *348*, 117–128.
- (48) Rampf, F.; Binder, K.; Paul, W. *J. Polym. Sci., Part B: Polym. Phys.* **2006**, *44*, 2542–2555.
- (49) Baysal, B. M.; Karasz, F. E. *Macromol. Theory Simul.* **2003**, *12*, 627–646.
- (50) Moore, M. A. *J. Phys. A: Math. Gen.* **1977**, *10*, 305.
- (51) Stockmayer, W. H. *Makromol. Chem.* **1960**, *35*, 54–74.
- (52) Muthukumar, M. In *Interphases and Mesophases in Polymer Crystallization III*; 2005; pp 241–274.
- (53) Binder, K.; Baschnagel, J.; Müller, M.; Paul, W.; Rampf, F. *Macromol. Symp.* **2006**, *237*, 128–138.
- (54) Zhou, Hall; Karplus, *Phys. Rev. Lett.* **1996**, *77*, 2822–2825.
- (55) Larini, L.; Barbieri, A.; Prevosto, D.; Rolla, P. A.; Leporini, D. *J. Phys.: Condens. Matter* **2005**, *17*, L199.
- (56) Muthukumar, M. In *Progress in Understanding of Polymer Crystallization*; **2007**, 1–18.
- (57) Doye, J. P. K.; Sear, R. P.; Frenkel, D. *J. Chem. Phys.* **1998**, *108*, 2134–2142.
- (58) Chen, C. M.; Higgs, P. G. *J. Chem. Phys.* **1998**, *108*, 4305–4314.
- (59) Swendsen, R. H.; Wang, J. *Phys. Rev. Lett.* **1986**, *57*, 2607.
- (60) Sugita, Y.; Okamoto, Y. *Chem. Phys. Lett.* **1999**, *314*, 141–151.
- (61) Geyer, C. J.; Keramidas, E. M. Keramidas, EM, Ed 156–163.
- (62) Sugita, Y.; Kitao, A.; Okamoto, Y. *J. Chem. Phys.* **2000**, *113*, 6042.
- (63) Wang, J. S.; Swendsen, R. H. *Progress of Theoretical Physics-Supplement* **2005**, 317–323.
- (64) Hukushima, K.; Nemoto, K. *J. Phys. Soc. Jpn.* **1996**, *65*, 1604–1608.
- (65) Hukushima, K.; Takayama, H.; Nemoto, K. *Int. J. Mod Phys C* **1996**, *7*, 337–344.
- (66) Hansmann, U. H. *Chem. Phys. Lett.* **1997**, *281*, 140–150.
- (67) Tesi, M. C.; Rensburg, E. J. J.; Orlandini, E.; Whittington, S. G. *J. Stat. Phys.* **1996**, *82*, 155–181.
- (68) Berg, B. A.; Neuhaus, T. *Phys. Lett. B* **1991**, *267*, 249–253.
- (69) Berg, Neuhaus *Phys. Rev. Lett.* **1992**, *68*, 9–12.
- (70) Berg, B. A.; Celik, T. *Phys. Rev. Lett.* **1992**, *69*, 2292.
- (71) Paul, W.; Müller, M. *J. Chem. Phys.* **2001**, *115*, 630.
- (72) Paul, W.; Müller, M. *Comput. Phys. Commun.* **2002**, *146*, 113–117.
- (73) Earl, D. J.; Deem, M. W. *Phys. Chem. Chem. Phys.* **2005**, *7*, 3910–3916.
- (74) Ryckaert, J. P.; Bellemans, A. *Faraday Discuss. Chem. Soc.* **1978**, *66*, 95–106.
- (75) Sundararajan, P. R.; Kavassalis, T. A. *J. Chem. Soc., Faraday Trans.* **1995**, *91*, 2541–2549.
- (76) Mayo, S. L.; Olafson, B. D.; Goddard, W. A. *J. Phys. Chem.* **1990**, *94*, 8897–8909.



- (77) Tobias, D. J.; Martyna, G. J.; Klein, M. L. *J. Phys. Chem.* **1993**, *97*, 12959–12966.
- (78) Trebst, S.; Troyer, M.; Hansmann, U. H. E. *J. Chem. Phys.* **2006**, *124*, 174903.
- (79) Katzgraber, H. G.; Trebst, S.; Huse, D. A.; Troyer, M. *J. Stat. Mech.* **2006**, 2006, P03018–P03018.
- (80) Nadler, W.; Hansmann, U. H. E. *Phys. Rev. E* **2007**, *76*, 057102.
- (81) Nadler, W.; Hansmann, U. H. E. *Phys. Rev. E* **2007**, *76*, 065701.
- (82) Nadler, W.; Hansmann, U. H. E. *J. Phys. Chem. B* **2008**, *112*, 10386–10387.
- (83) Sindhikara, D. J.; Emerson, D. J.; Roitberg, A. E. *J. Chem. Theory Comput.* **2010**, *6*, 2804–2808.
- (84) Kone, A.; Kofke, D. A. *J. Chem. Phys.* **2005**, *122*, 206101.
- (85) Rosta, E.; Hummer, G. *J. Chem. Phys.* **2009**, *131*, 165102.
- (86) Li, T.; Jiang, Z.; Yan, D.; Nies, E. *Polymer* **2010**, *51*, 5612–5622.
- (87) Ivanov, V. A.; Paul, W.; Binder, K. *J. Chem. Phys.* **1998**, *109*, 5659.
- (88) Higgins, J. *Polymers and neutron scattering*; Clarendon Press: Oxford, 1996.
- (89) Destree, M.; Lyulin, A.; Ryckaert, J. *Macromolecules* **1996**, *29*, 1721–1727.
- (90) Sundararajan, P. R.; Kavassalis, T. A. *Faraday Trans.* **1995**, *91*, 2541.
- (91) Doye, J. P. K.; Sear, R. P.; Frenkel, D. *J. Chem. Phys.* **1998**, *108*, 2134.
- (92) Noguchi, H.; Yoshikawa, K. *J. Chem. Phys.* **1998**, *109*, 5070.
- (93) Yoshikawa, K.; Yoshinaga, N. *J. Phys.: Condens. Matter* **2005**, *17*, S2817–S2823.
- (94) Odijk, T. *Macromolecules* **1993**, *26*, 6897–6902.
- (95) Cifra, P.; Benková, Z.; Bleha, T. *J. Phys. Chem. B* **2008**, *112*, 1367–1375.
- (96) Sarraguça, J. M. G.; Dias, R. S.; Pais, A. A. C. C. *J. Biol. Phys.* **2006**, *32*, 421–434.
- (97) Stukan, M. R.; Ivanov, V. A.; Grosberg, A. Y.; Paul, W.; Binder, K. *J. Chem. Phys.* **2003**, *118*, 3392.
- (98) Hud, N. V.; Vilfan, I. D. *Annu. Rev. Biophys. Biomol. Struct.* **2005**, *34*, 295–318.
- (99) Stukan, M.; An, E.; Ivanov, V.; Vinogradova, O. *Phys. Rev. E* **2006**, *73*.
- (100) Vasilevskaya, V. V.; Khokhlov, A. R.; Kidoaki, S.; Yoshikawa, K. *Biopolymers* **1997**, *41*, 51–60.
- (101) Ivanov, V. A.; Stukan, M. R.; Vasilevskaya, V. V.; Paul, W.; Binder, K. *Macromol. Theory Simul.* **2000**, *9*, 488–499.
- (102) Narambuena, C.; Leiva, E.; Chávez-Páez, M.; Pérez, E. *Polymer* **2010**, *51*, 3293–3302.

CT100513Y